Research Article | Open Access

Microstructures

Khan *et al. Microstructures* **2026**, *6*, 20260141 **DOI:**10.20517/microstructures.2026.128

Engineering Si-bridge mediated g-C_3N_4/$NdFeO_3$ Z-scheme heterojunction for multifunctional catalytic applications: CO_2 conversion, organic pollutant degradation and H_2 production

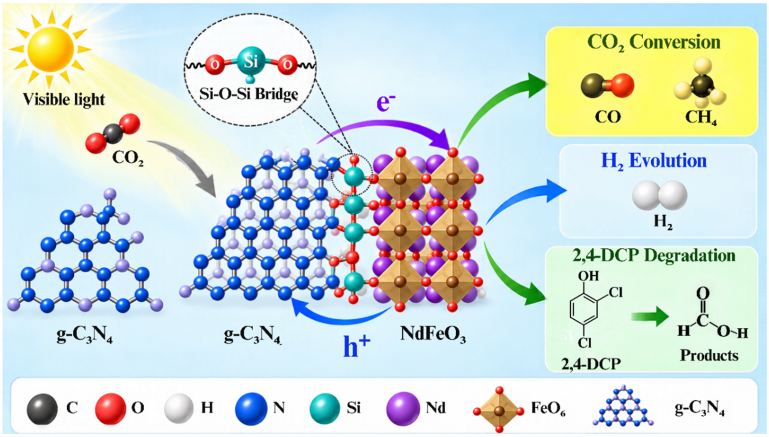
Iltaf Khan[1,#], Saeed Zaman[2,#], Ali Bahadur[3], Anuj Kumar[4], Safura Bibi[5], Muhammad Hammad Zaman[6], Laiba Mujahid[7], Ghulam Yasin[8], Aftab Khan[9], Shoaib Khan[10]

Keywords:
$NdFeO_3$ nanosheets, energy fuels, photoelectrons modulation, CO_2 reduction, 2,4-DCP degradation, methanol-assisted H_2 generation

Citation: Khan, I.; Zaman, S.; Bahadur, A.; Kumar, A.; Bibi, S.; Zaman, M. H.; Mujahid, L.; Yasin, G.; Khan, A.; Khan, S. Engineering Si-bridge mediated g-C_3N_4/$NdFeO_3$ Z-scheme heterojunction for multifunctional catalytic applications: CO_2 conversion, organic pollutant degradation and H_2 production. *Microstructures* **2026**, *6*, 20260141. https://dx.doi.org/10.20517/microstructures.2026.128

Received: 3 Jun 2026 **First Decision:** 10 Jul 2026 **Revised:** 17 Oct 2026 **Accepted:** 20 Oct 2026 **Published:** 11 Nov 2026

Academic Editor: Zhanxi Fan
Copy Editor: Fangling Lan
Production Editor: Fangling Lan



Abstract

Environmental pollution and rapid consumption of energy and fuel resources are two major issues in the modern world. To address these issues, we engineered a silicate-bridged g-C_3N_4/$NdFeO_3$ Z-scheme nanocomposite and used it for photocatalytic CO_2 conversion, 2,4-DCP degradation, and methanol-assisted H_2 evolution. Compared to $NdFeO_3$ and g-C_3N_4 nanoparticles, the $NdFeO_3$ and g-C_3N_4 nanosheets, respectively, have larger surface areas, developed morphologies, enhanced charge separation, and improved photocatalytic performance. Remarkably, the introduction of g-C_3N_4 nanosheets into $NdFeO_3$ nanosheets (NFONS) effectively optimizes the band gap position, promotes charge separation through a Z-scheme electron-transfer mechanism, enlarges the surface area, and improves photocatalytic efficiency. In addition, the silicate (Si-O) bridge served as an electronic bridge charge-transfer facilitator, resolved lattice mismatch, and enhanced photocatalytic efficiency by modulating photoelectrons. Compared with pristine NFONS, the optimized 5CNNS-1.5Si/NFONS nanocomposites delivered a 14.17-fold improvement in CO_2 conversion activity, a 7.25-fold increase in photocatalytic 2,4-DCP degradation, and a 2.64-fold increase in methanol-assisted H_2 generation. Scavenger experiments and the photocatalytic pollutant degradation mechanism confirmed that photogenerated holes (h^+)

[1]School of Chemical Science and Engineering, Tongji University, Shanghai 200092, China.
[2]School of Materials Science and Engineering, Harbin Institute of Technology (Shenzhen), Shenzhen 518055, Guangdong, China.
[3]Department of Chemistry, College of Science, Mathematics, and Technology, Wenzhou-Kean University, Wenzhou 325060, Zhejiang, China.

[4]Nano-Technology Research Laboratory, Department of Chemistry, GLA University, Mathura 281406, India.
[5]Department of Botany, University of Agriculture Faisalabad, Faisalabad 38040, Pakistan.
[6]School of Chemical Engineering and Technology, Tianjin University, Tianjin 300350, China.
[7]School of Environmental & Chemical Engineering, Jiangsu University of Science and Technology, Zhenjiang 212100, Jiangsu, China.
[8]School of Environment and Civil Engineering, Dongguan University of Technology, Dongguan 523808, Guangdong, China.
[9]State Key Laboratory of Chemical Resource Engineering, Beijing Advanced Innovation Center for Soft Matter Science and Engineering, College of Chemistry, Beijing University of Chemical Technology, Beijing 100029, China.
[10]Jiangsu Key Laboratory of Sericultural and Animal Biotechnology, School of Biotechnology, Jiangsu University of Science and Technology, Zhenjiang 212100, Jiangsu, China.
[#]Authors contributed equally.

Correspondence to: Prof. Iltaf Khan, School of Chemical Science and Engineering, Tongji University, Shanghai 200092, China. E-mail: doctoriltafkhan@tongji.edu.cn; Dr. Ali Bahadur, Department of Chemistry, College of Science, Mathematics, and Technology, Wenzhou-Kean University, Wenzhou 325060, Zhejiang, China. E-mail: Abahadur@wku.edu.cn

and superoxide radicals ($\bullet O_2^-$) are the dominant reactive species that initiate the photocatalytic activities. Our findings offer valuable insights into the design of Z-scheme nanocomposites and their employment for multifunctional photocatalytic applications.

INTRODUCTION

Environmental pollution and the energy crisis are two major global issues. The emission of CO_2 and toxic organic pollutants, such as 2,4-dichlorophenol (2,4-DCP), poses a serious threat to the environment[1]. 2,4-DCP is well known to be carcinogenic and is frequently found in industrial wastewater[2]. Moreover, green hydrogen production can offer an alternative to fossil fuels and address the ongoing energy crisis[3]. In this regard, the development of efficient, affordable, and environmentally friendly strategies for CO_2 reduction, organic pollutant degradation, and production of green energy fuels is crucial[4].

Recently, nanotechnology and photocatalysis have emerged as prominent strategies to address environmental pollution and the energy crisis[5]. Similarly, semiconductor-based catalysts can convert CO_2 into valuable fuels, produce H_2, and degrade organic pollutants by utilizing solar energy[6,7]. It is well known that the major part of the solar spectrum is visible light (~50%)[8]. Therefore, it is highly challenging to find suitable visible-light-active materials that can work under visible light and effectively utilize the abundant solar light[9].

Among visible light-active nanocatalysts, $NdFeO_3$ (NFO) has gained tremendous attention and emerged as a potential material in different sectors, owing to its distinctive electronic structure, non-toxic characteristics, and appropriate energy band gap (~2.0 to 2.2 eV)[10,11]. Nonetheless, the overall efficiency of NFO is hindered by multiple factors, such as a small surface area, inadequate morphology, fewer active sites, positive conduction band position, and low charge separation[12]. Therefore, controlling NFO morphology is a suitable approach to address these limitations by increasing surface area and enhancing photocatalytic activity. Notably, $NdFeO_3$ nanosheets (NFONS) offer abundant reactive sites, a large surface area, and shorter distances for transferring photogenerated carriers compared with NFO nanoparticles. However, the positive conduction band of NFONS and poor charge separation still limit their photocatalytic efficiency. Therefore, developing a Z-scheme heterojunction is an effective approach to enhance charge separation and activate photogenerated charge carriers[13]. The Z-scheme heterojunction of p-type $NdFeO_3$ with n-type g-C_3N_4 improves charge separation and shifts it to the visible region, leading to improved photocatalytic performance[14,15]. Very recently, Z-scheme heterojunctions have attracted considerable attention and considered an effective strategy for simultaneously addressing organic pollutants and energy crises[16]. In addition, g-C_3N_4 nanosheets (CNNS) offer several advantages, including superior visible-light absorption, a high surface-to-volume ratio, and enhanced photocatalytic activity compared with g-C_3N_4 nanoparticles

(CNNP). Thus, the more negative CB position and high surface area of CNNS make them a good choice for designing Z-scheme heterojunctions and improving NFONS efficiency[17]. However, the interfacial mismatch between these semiconductors (g-C_3N_4 and $NdFeO_3$) remains a critical issue. Very recently, electronic bridges (Si-O, Mg-O, and Al-O)[18] can address this issue and enhance efficient electron flow across lattice-mismatch materials. With this in mind, we introduced a silicate (Si-O) bridge into the CNNS/NFONS heterojunction, which acts as an interfacial electronic channel and bridge that promotes charge migration, serving as both a linker and a charge-transfer facilitator. In short, this approach resolves the lattice-mismatch issue and improves photocatalytic efficiency[19,20].

In our current research, we successfully engineered a Si-bridge-mediated g-C_3N_4/$NdFeO_3$ Z-scheme heterojunction and employed it for multifunctional catalytic applications. Our findings will provide new insights into the synthesis of $NdFeO_3$-based materials and their potential applications in pollutant degradation and sustainable energy production.

EXPERIMENTAL

Materials preparation

All starting materials and reagents utilized in the research were of analytical grade, and the experiments were conducted with deionized water that had been subjected to double distillation. The reagents utilized include Ethanol (C_2H_5OH), ethylene glycol ($HOCH_2CH_2OH$), sodium hydroxide (NaOH), nitric acid (HNO_3), polyvinylpyrrolidone (PVP), 2,4-dichlorophenol ($C_6H_4Cl_2O$), and urea ($CO(NH_2)_2$) were purchased from Aladdin Group Co., Ltd. Iron(III) nitrate nonahydrate ($Fe(NO_3)_3·9H_2O$), neodymium(III) nitrate hexahydrate ($Nd(NO_3)_3·6H_2O$), sodium silicate (Na_2SiO_3), and methanol (CH_3OH) were purchased from Sinopharm Chemical Reagent Co., Ltd, Sigma Aldrich Merck Ltd, China with standard purity and utilized without additional purification.

Synthesis of NFONS

NFONS were synthesized by a hydrothermal method; the detailed synthesis scheme is shown in Supplementary Figure 1A. In the standard experiment, $Nd(NO_3)_3·6H_2O$ (4.82 g, 11.0 mmol) and $Fe(NO_3)_3·9H_2O$ (4.44 g, 11.0 mmol) were dissolved in a mixed solvent of 55 mL DI water, 25 mL ethanol, and 30 mL methanol. Next, an equal molar solution of PVP was added, and the mixture was stirred at 400 rpm for 1 h to yield a clear reddish solution. After this, the solution was divided equally between two 100 mL Teflon-lined stainless-steel autoclaves (55 mL each) and heated at 180 °C for 12 h in an oven to complete the hydrothermal reaction. After cooling to room temperature, the product was well washed 3 times with ethanol and deionized water. Next, the as-received product was dried in an oven at 80 °C overnight and then calcined for 2 h in a muffle furnace at 500, with a heating rate of 4 °C per min[21].

Synthesis of CNNS

We obtained CNNS by calcination, as shown in Supplementary Figure 1B. In a standard experiment, 15 g of urea was placed in a ceramic crucible and heated in a muffle furnace at 550 °C for 4 h at a rate of 5 °C min^{-1} (ramp time ≈ 105 min). The furnace was then allowed to cool naturally to room temperature. The collected samples were treated 5 times with 0.2 M HNO_3, and then rinsed 3 times with water and absolute ethanol. The purified samples were then dried in an oven at 80 °C for 12 h. Finally, the resulting yellowish product was ground to a fine powder[22].

Synthesis of g-C_3N_4 nanosheet/$NdFeO_3$ nanosheet Z-scheme nanocomposites

We synthesized the g-C_3N_4 nanosheet/$NdFeO_3$ nanosheet Z-scheme nanocomposites by a wet chemical method. In the standard experiment, we mixed different amounts of CNNS with the as-prepared NFONS. In a typical procedure, 1 g of NFONS was dispersed in a 100 mL ethanol-water mixture (1:1, v/v). Subsequently,

a defined mass of CNNS corresponding to the desired mass ratios (1%, 3%, 5%, and 7%) was added to the NFONS dispersion. The resulting mixture was ultrasonicated for 1 h to obtain a homogeneous dispersion and enhance interfacial contact between the CNNS and NFONS. After ultrasonication, the mixture was stirred continuously at 400 rpm for 4 h at 85.0 °C. Once the solvent was evaporated completely, the powder-form composite was then dried in an oven at 80 °C to remove residual solvents. Finally, the dried material was calcined at 400 °C for 120 min in air, at a heating rate of 5 °C min^{-1}, to remove impurities, improve interfacial bonding, and strengthen the structural features of the composite[23]. Remarkably, the resulting products were denoted as XCNNS/NFONS, where X denotes the mass percentage ratio of CNNS to NFONS.

Fabrication of Si-bridge-mediated g-C_3N_4/$NdFeO_3$ Z-scheme heterojunction

Si-Bridge-mediated g-C_3N_4/$NdFeO_3$ Z-scheme heterojunction was synthesized in two steps; the comprehensive synthesis scheme is given in Supplementary Figure 1C. In the 1st step, 0.99 g of as-synthesized NFONS were dispersed in 100 mL of 1.0 M aqueous sodium silicate (Na_2SiO_3) solution (1.0 M sodium silicate solution was prepared by dissolving 12.21 g of Na_2SiO_3 in 100 mL of distilled water). The suspension was vigorously stirred for 1 h to facilitate silicate-ion adsorption onto the NFONS surface, forming a silicate bridge. After stirring, the mixture was filtered, and the collected product was dried in an oven at 85 °C for 12 h. The resultant silicate-modified NFONS was labeled as YSi/NFONS, where Y denotes the mole ratio of Si bridge to NFONS. In the 2nd step, 1.0 g of silicate bridge-modified NFONS (YSi/NFONS) was mixed with 0.05 g of previously prepared CNNS in an ethanol-water mixture (1:1, v/v). The mixture was stirred at 85 °C for 4 h. The resulting products were dried in an oven at 80 °C for several hours to remove impurities. Finally, the dried products were calcined in air at 400 °C for 2 h at a ramp rate of 5 °C/min[15]. Additionally, other experimental methods are described in the Supplementary Materials, and a list of abbreviations and acronyms used throughout this manuscript is provided in Supplementary Table 1.

RESULTS AND DISCUSSION

In this research, we synthesized silicate-bridged g-C_3N_4/$NdFeO_3$ nanosheet-based Z-scheme nanocomposites, which exhibit exceptional visible-light photocatalytic activities for CO_2 conversion, 2,4-DCP degradation, and H_2 generation. Our findings proved that NFONS and CNNS demonstrate superior performance in terms of surface area, charge separation, and activities compared to $NdFeO_3$ nanoparticles (NFONP) and g-C_3N_4, respectively. Remarkably, the introduction of g-C_3N_4 nanosheets into NFONS effectively optimizes the band gap position, promotes charge separation through a Z-scheme electron-transfer mechanism, enlarges surface area, and improves photocatalytic efficiency. In addition, the introduction of a silicate (Si-O) bridge served as an electronic bridge, a charge-transfer facilitator, resolved lattice mismatch, and accordingly enhanced photocatalytic efficiency and modulated photoelectrons.

Comparative investigation of NFONS and NFONP

Here, we successfully prepared NFONS, which have a unique structure, high surface area, enhanced charge separation, and improved multifunctional activities as compared to NFONP. The transmission electron microscopy (TEM) image of NFONP [Figure 1A] and the scanning electron microscopy (SEM) image of NFONP [Supplementary Figure 2A] reveal that these structures show aggregation and that the nanoparticles are packed, which hinders their overall performance. In contrast, the TEM image of NFONS [Figure 1B] and the SEM image of NFONS [Supplementary Figure 2B] show well-exfoliated nanosheets with plenty of empty, active space and well-arranged structures, which increase surface area and, accordingly, overall performance. The XRD patterns [Figure 1C] reveal that NFONS exhibit well-defined diffraction peaks, indicating good crystallinity and a well-arranged crystal structure as compared to NFONP. The peaks located at 22.8°, 25.1°, 27.4°, 34.0°, 40.1°, 41.9°, 46.5°, 48.0°, 53.1°, 58.4°, 64.0°, 68.2°, 73.4°, and 77.7° corresponding to (110), (111), (121), (210), (031), (022), (202), (040), (131), (123), (133), (242), (143), and (420) crystal planes, which confirm the successful synthesis of $NdFeO_3$ phase (JCPDS card no. 01-082-2421)[24]. In addition, the

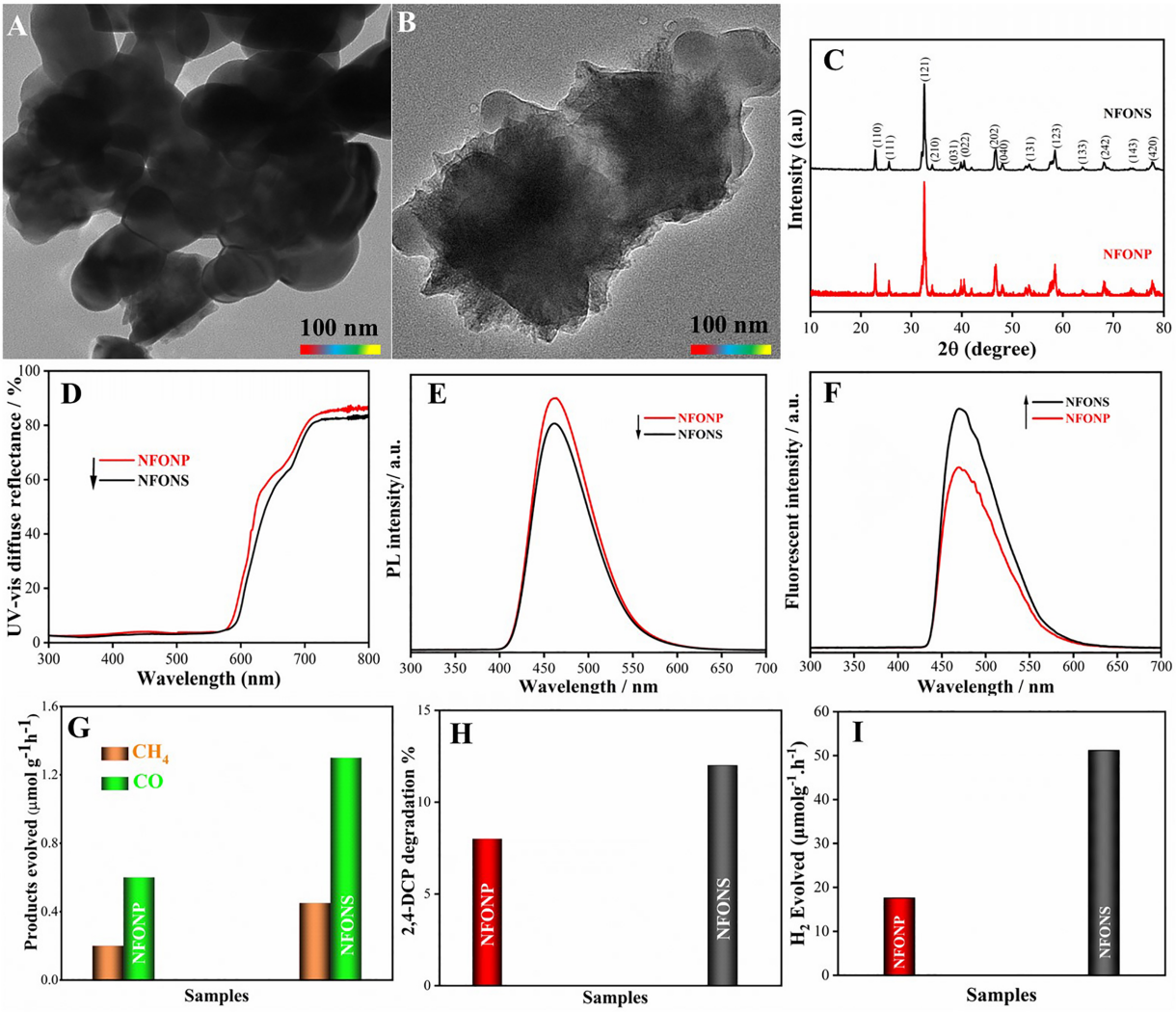


Figure 1. TEM images (A and B), XRD patterns (C), UV-Vis diffuse reflectance spectra (D), PL spectra (E), Fluorescence spectra reacted with coumarin, a fluorescent probe for •OH (F), Photocatalytic activities for CO_2 reduction (G), 2,4-DCP degradation activities (H), and Hydrogen generation (I) of NFONS and NFONP.

ultraviolet-visible diffuse reflectance spectroscopy (UV-Vis DRS) spectra [Figure 1D] illustrate that the NFONS band edge is located within the visible light region as compared to NFONP, which means that NFONS have a narrow band gap as compared to NFONP. Furthermore, the photoluminescence (PL) spectra [Figure 1E] and fluorescence spectra (FS) related to •OH radicals [Figure 1F] confirm that NFONS possess superior charge separation as compared to NFONP.

In practice, comparative multifunctional photocatalytic activity studies showed that NFONS delivered 2.19 times higher CO_2 conversion [Figure 1G], 1.50-fold higher 2,4-DCP degradation [Figure 1H], and a 2.9-fold increase in H_2 generation [Figure 1I] compared with NFONP[25,26]. Based on these findings, NFONS show well-defined morphology, good crystal structure, enhanced charge separation, more visible-light activity, and improved photocatalytic activity compared with NFONP[27].

An in-depth comparison of CNNS and CNNP

In this phase of our research, we successfully synthesized CNNS by heating urea; remarkably, slow calcination (5 °C min^{-1}) yielded well-exfoliated, high-surface-area CNNS. Our study shows that these CNNS have a markedly larger surface area, better morphology, more pores, and improved photocatalytic

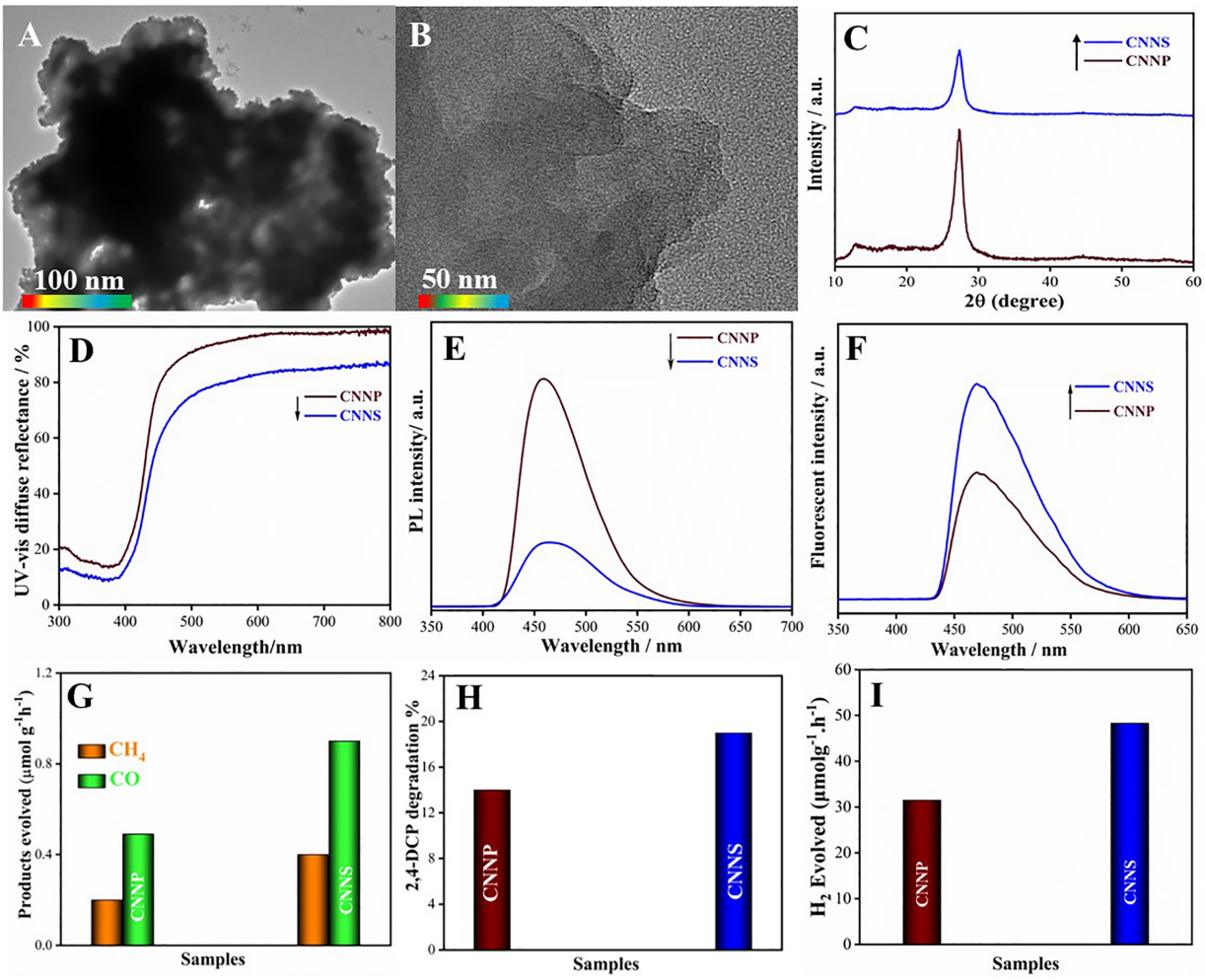


Figure 2. TEM images (A and B), XRD patterns (C), UV-Vis diffuse reflectance spectra (D), PL spectra (E), Fluorescence spectra reacted with coumarin, a fluorescent probe for •OH (F), Photocatalytic activities for CO_2 conversion (G), 2,4-DCP degradation (H), and Hydrogen generation activities (I) of CNNS and CNNP.

performance than CNNP[28]. In short, our experimental results demonstrated that CNNS offer exceptional performance over CNNP. The TEM image of CNNP [Figure 2A] shows aggregation and that the nanoparticles are packed, which hinders their overall performance, while the TEM image of CNNS [Figure 2B] indicates well-exfoliated nanosheets, plenty of empty and active space, and well-arranged structures, which will increase their surface area and, accordingly, their overall performance. The XRD patterns for CNNS and CNNP are shown in Figure 2C and exhibit similar peaks, suggesting that the two materials have similar crystal structures. In addition, the UV-Vis DRS spectroscopy displayed in Figure 2D illustrates that the CNNS band edge is located within the visible light region as compared to CNNP, which means that CNNS have a narrow band gap as compared to CNNP. Furthermore, the PL spectra [Figure 2E] and FS spectra related to •OH radicals [Figure 2F] confirm that CNNS possess superior charge separation as compared to CNNP[29]. Compared to CNNP, the CNNS delivered higher multifunctional photocatalytic activities for CO_2 conversion [Figure 2G], 2,4-DCP degradation [Figure 2H], and H_2 evolution [Figure 2I]. To put it briefly, the findings of these studies confirmed that CNNS demonstrate a large surface area, more porosity, enhanced charge separation, well-exploited sheets, and improved multifunctional photocatalytic activities as compared to CNNP[30].

Comprehensive investigations of g-C_3N_4/NFONS Z-Scheme heterojunction

As discussed above, the visible light activity of the existing NFONS is still not satisfactory, mainly due to small surface area, low charge separation, and a positive CB. To address these issues, we modified the as-synthesized NFONS by coupling them with CNNS. This Z-scheme heterojunction increased reactive sites, expanded the specific surface area, improved the surface-to-volume ratio, adjusted band gaps for photogenerated carrier transfer, provided more robust thermodynamic stabilization, and finally improved the multifunctional photocatalytic activity. XRD patterns were recorded to check the crystal nature and structural properties of the prepared sample. It can be observed from XRD patterns given in Figure 3A that the peaks located at 22.8°, 25.1°, 27.4°, 34.0°, 40.1°, 41.9°, 46.5°, 48.0°, 53.1°, 58.4°, 64.0°, 68.2°, 73.4°, and 77.7° corresponding to (110), (111), (121), (210), (031), (022), (202), (040), (131), (123), (133), (242), (143), and (420) crystal planes, which confirms the successful synthesis of $NdFeO_3$ phase (JCPDS card no. 01-082-2421)[24]. The identified peaks align with the respective phases[31,32]. Remarkably, CNNS exhibits distinct diffraction peaks at approximately 12.8° and 27.4°, corresponding to the (100) and (002) crystallographic planes of g-C_3N_4, respectively[33]. Notably, the XRD patterns of the resulting heterojunction retain the primary diffraction peaks of NFONS as well as the characteristic diffraction peaks of g-C_3N_4, confirming that both crystalline phases coexist within the CNNS/NFONS composite without substantial structural distortion of either component. In addition, UV-Vis DRS [Figure 3B] shows a slight shift of NFONS absorption toward the visible region upon CNNS incorporation, suggesting enhanced light-absorption properties. It can be seen that after CNNS incorporation, the band edges shift to longer wavelengths and into the more visible region, and accordingly the band gap decreases, which will not enhance charge separation, but the resulting samples will also absorb more light and, finally, photocatalytic activities will increase. PL spectra serve as a valuable tool for evaluating the recombination rates of photogenerated charge carriers. Generally, PL signals arise from charge recombination upon light excitation, thereby establishing a direct correlation between the PL response intensity and the enhancement of charge separation. In short, a more intense PL signal generally indicates low charge separation, while a less intense PL signal implies enhanced charge separation. Figure 3C shows that the PL intensity of NFONS gradually decreases as CNNS content increases. Notably, the 5CNNS/NFONS nanocomposite exhibits the lowest PL intensity, indicating the highest charge-separation efficiency and suggesting the most effective photocatalytic performance. These results are further verified by FS associated with the •OH generation; it can be seen from Figure 3C inset that the FS response is increased after adding XCNNS, and the 5CNNS/NFONS showed the highest response, confirming the best sample[34]. For practical applications, we checked the photocatalytic capability of NFONS and XCNNS/NFONS nanocomposites for CO_2 reduction, 2,4-DCP degradation, and H_2 generation under visible-light irradiation in an aqueous medium, without co-catalysts.

It can be observed from Figure 3D that NFONS have low photocatalytic activity for CO_2 conversion into CH_4 (0.45 μmol $g^{-1}h^{-1}$) and CO (1.30 μmol $g^{-1}h^{-1}$). However, photocatalytic performance improved markedly when coupled with different amounts of CNNS. As compared to other prepared samples, the 5CNNS/NFONS nanocomposite showed a 6.80-fold improvement in photocatalytic activity by producing CH_4 (3.10 μmol $g^{-1}h^{-1}$) and CO (8.80 μmol $g^{-1}h^{-1}$). Similarly, the as-prepared samples were evaluated for photocatalytic 2,4-DCP degradation [Figure 3E]. The 5CNNS/NFONS showed the highest activity (59.0%). Similarly, as shown in Figure 3F, 5CNNS/NFONS generated 95.7 μmol $g^{-1}h^{-1}$ hydrogen, which is 1.87 times higher than NFONS (51.20 μmol $g^{-1}h^{-1}$). The findings unequivocally indicate that integrating CNNS markedly improves the photocatalytic efficiency of pristine NFONS. In light of these findings, it is confirmed that the coupling of CNNS with NFONS and forming a Z-scheme heterojunction fruitfully increased reactive sites, expanded the specific surface area, improved the surface-to-volume ratio, adjusted band gaps for photogenerated carrier transfer, provided more robust thermodynamic stabilization, enhanced charge separation and finally improved the multifunctional photocatalytic activities for CO_2 conversion, 2,4-DCP degradation and H_2 generation.

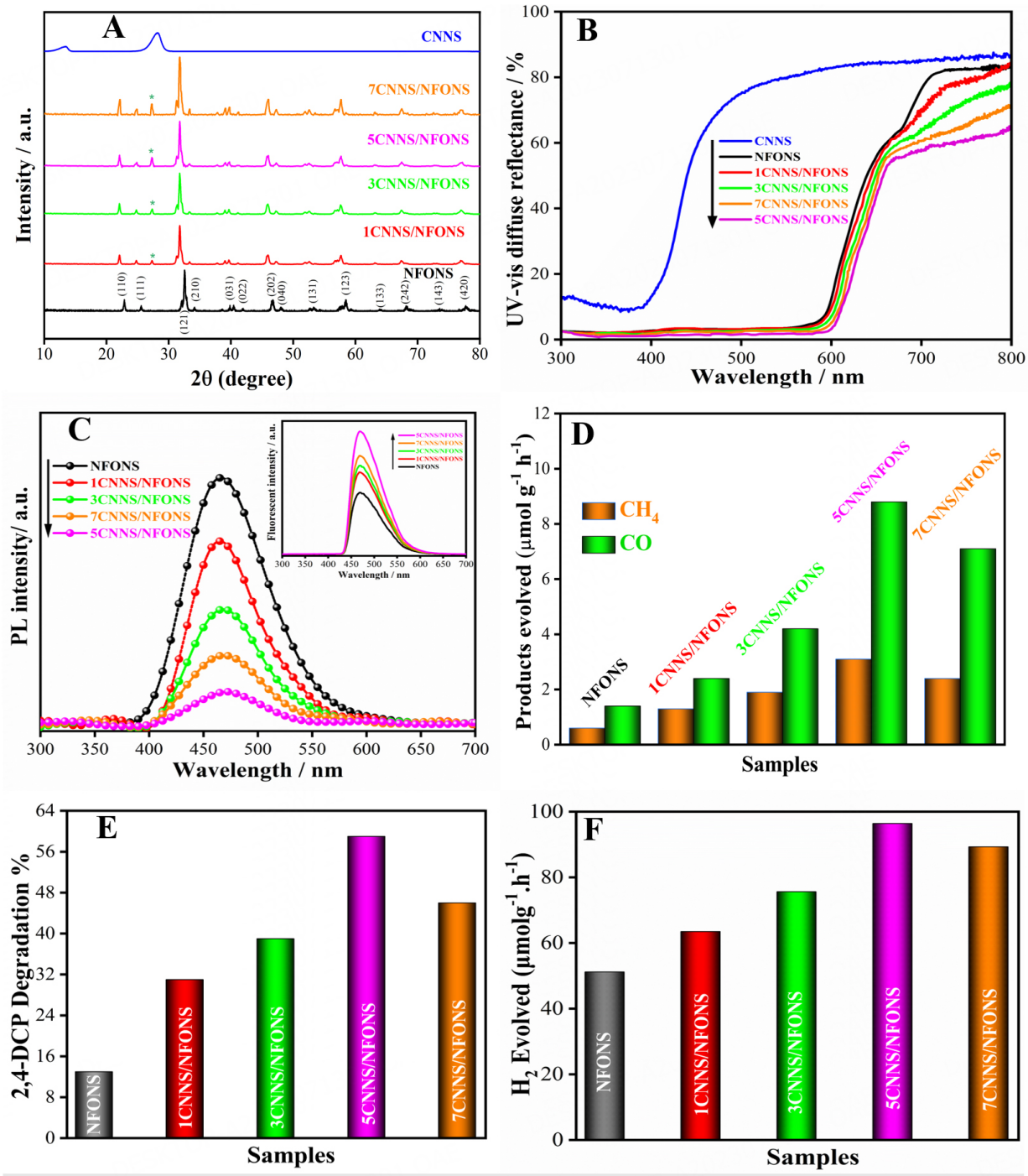


Figure 3. XRD patterns (A), UV-Vis diffuse reflectance spectra (B), PL emission spectra with inset FS spectra linked with •OH (C), Photocatalytic activities for CO_2 conversion (D), 2,4-DCP degradation (E), and Hydrogen evolution (F) of NFONS and XCNNS/NFONS.

Integration of Si-bridge into g-C_3N_4 Z-scheme heterojunction as an interfacial linker and electron transfer mediator

The interfacial mismatch between n-type g-C_3N_4/p-type NFONS was solved by introducing a (Si-O) bridge, which acts as an interfacial electronic channel and electronic bridge that promotes charge migration, serving both as a linker and a charge-transfer facilitator. In short, this approach resolves the lattice-mismatch issue and finally improves photocatalytic efficiency[35].

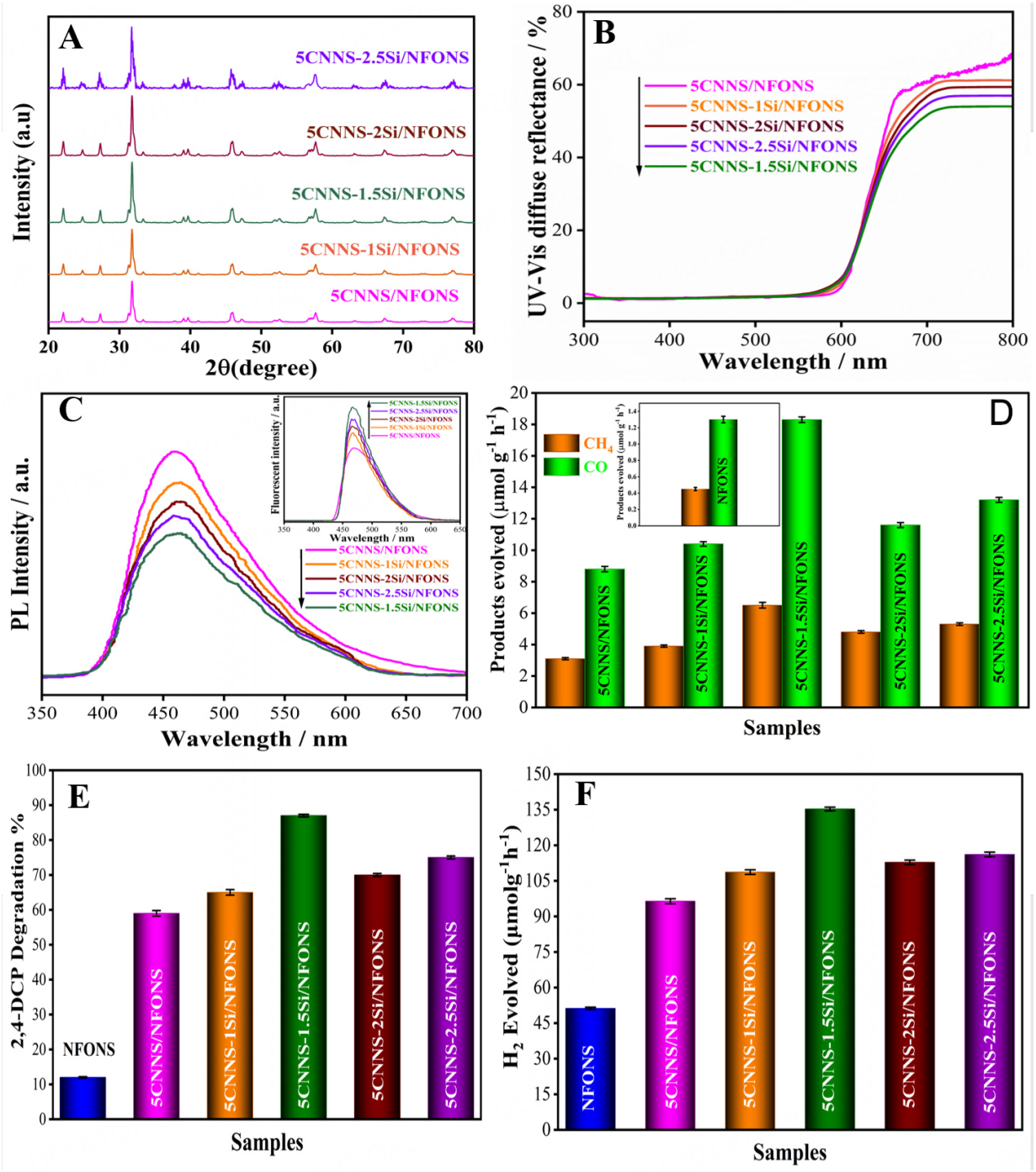


Figure 4. XRD patterns (A), UV-Vis diffuse reflectance spectra (B), PL emission spectra with FS inset spectra (C), and photocatalytic activities for CO_2 conversion (D), 2,4-DCP degradation (E), and H_2 evolution (F) of pristine NFONS and 5CNNS-YSi/NFONS. Error bars in (D-F) represent the standard deviation of four independent measurements (n = 4).

Aiming to investigate the composite system, various types of characterization were carried out. The XRD patterns displayed in Figure 4A and the UV-Vis spectra given in Figure 4B demonstrate that the incorporation of the Si-O bridge does not alter the crystallinity and the band edges, respectively. In addition, the lowest PL intensity [Figure 4C] and highest FS associated with the •OH generation (Figure 4C inset) confirm that the incorporation of the Si-O bridge effectively enhances charge separation, and among the samples, 5CNNS-1.5Si/NFONS showed the highest response. Figure 4D, with standard-deviation error bars,

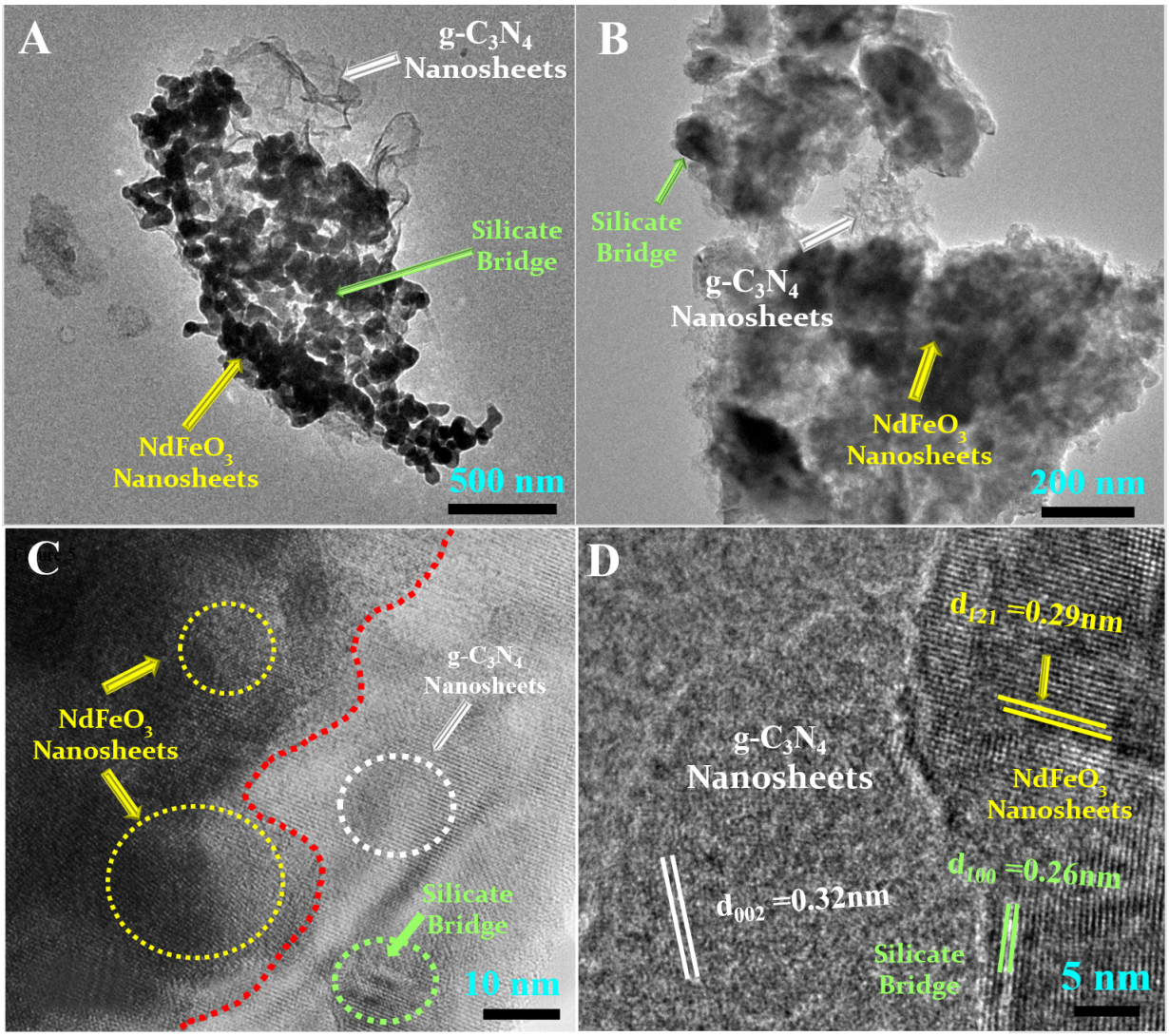


Figure 5. TEM images (A and B), HRTEM images (C and D) of the 5CNNS-1.5Si/NFONS nanocomposites.

shows that the 5CNNS-1.5Si/NFONS composite exhibited 14.17-fold and 2.08-fold increases in activity as compared to NFONS and 5CNNS/NFONS, respectively. Similarly, the as-prepared samples were checked for photocatalytic 2,4-DCP degradation [Figure 4E] (as standard deviation error bars). The most active 5CNNS-1.5Si/NFONS showed a 7.25-fold increase. Additionally, the 5CNNS-1.5Si/NFONS generated 2.64-fold more hydrogen compared with NFONS, as standard deviation error bars are shown [Figure 4F]. Notably, if the amount of introduced Si-O or CNNS content is further increased, a decline in photocatalytic performance occurs, which means that the 5CNNS-1.5Si/NFONS is an optimized sample[36].

The reproducibility, stability, and recyclability of the photocatalytic performance were further verified through 4 independent measurements. The consistent CH_4 production [Supplementary Figure 3A], CO production [Supplementary Figure 3B], 2,4-DCP degradation [Supplementary Figure 3C], and H_2 evolution rates [Supplementary Figure 3D] were observed. To confirm reproducibility, four independent runs (n = 4) were conducted for all samples; the mean ± standard deviation values are given in Supplementary Table 2[37].

Catalyst stability strongly affects photocatalytic performance. With this aim, XRD patterns, photocatalytic activities, stability, and reusability were evaluated for 5CNNS-1.5Si/NFONS[38]. Supplementary Figure 4A and B, Supplementary Figure 5A and B show that the sample recovered after

different characterizations and catalytic reactions maintained a similar physical appearance in terms of color as well as weight after four consecutive cycles. In addition, thermogravimetric analysis (TGA) shown in Supplementary Figure 5C confirms that before and after different characterizations and catalytic reactions, the corresponding TGA curves exhibit nearly identical weight-loss profiles and decomposition patterns. These results confirmed that the composite structure remained stable. Furthermore, UV-Visible absorption spectra [Supplementary Figure 5D] confirm that the recovered catalyst showed no notable changes before and after different characterizations and catalytic reactions. Thus, it is confirmed that our samples have excellent structural and physicochemical stability during the photocatalytic process.

Based on the aforementioned findings, it has been confirmed that, among the prepared samples, the 5CNNS-1.5Si/NFONS is the most active and amount-optimized sample. Similarly, 5CNNS-1.5Si/NFONS shows enhanced charge separation, a larger surface area, a well-designed structure, and improved multifunctional photocatalytic activity. So, the morphology of this sample is further investigated. The TEM images are depicted in Figure 5A and B, showing that NFONS and CNNS exhibit a sheet-like morphology, and these closely assembled structures give an enlarged surface area and active sites for multifunctional applications. In addition, the high-resolution transmission electron microscopy (HRTEM) [Figure 5C and D] shows lattice fringes with interplanar spacings of 0.32, 0.29, and 0.26 nm, corresponding to g-C_3N_4 (002), $NdFeO_3$ (121), and Si-O bridge (100), respectively. Remarkably, the coexistence of these lattice features, together with the observed interfacial contact, supports the successful assembly of the composite structure. Notably, the Si-O bridge may facilitate interfacial charge transfer and photoelectron modulation between g-C_3N_4 and $NdFeO_3$[39].

IN-DEPTH ELUCIDATION OF THE MECHANISM

Here, we engineered a silicate-bridged g-C_3N_4/$NdFeO_3$ Z-Scheme nanocomposite and employed it for photocatalytic CO_2 conversion, 2,4-DCP degradation, and methanol-assisted H_2 evolution. NFONP exhibit restricted photocatalytic applications mainly due to their considerable size and tendency for particle aggregation. Remarkably, this issue was addressed by synthesizing NFONS using PVP as a stabilizing ligand and morphological regulator[40]. Notably, the shift in morphology from nanoparticles to nanosheets markedly improved the overall efficiency of $NdFeO_3$. Nonetheless, the visible light activity of the existing NFONS is still not satisfactory, mainly due to small surface area, low charge separation, and a positive CB. To address these issues, we modified the as-synthesized NFONS by coupling them with CNNS. Fruitfully, making such a Z-scheme heterojunction increased reactive sites, expanded the specific surface area, improved the surface-to-volume ratio, adjusted band gaps for photogenerated carrier transfer, provided more robust thermodynamic stabilization, and finally improved the multifunctional photocatalytic activity. The interfacial mismatch between CNNS and NFONS was addressed by introducing a (Si-O) bridge, which acts as an interfacial electronic channel that promotes charge migration and serves both as a linker and a charge-transfer facilitator. In short, this approach resolves the lattice-mismatch issue and finally improves photocatalytic efficiency[41]. The design strategy of the resultant Z-scheme is illustrated in Figure 6A. It can be observed that the conduction band (CB) and valence band (VB) potentials of CNNS are approximately -1.3 and +1.4 eV, respectively, whereas the CB and VB potentials of NFONS are approximately +0.27 and +2.23 eV, respectively[42]. Thus, the Z-scheme heterojunction of p-type $NdFeO_3$ with n-type g-C_3N_4 improves charge separation, adjusts band-gap position, increases surface area, and accordingly improves photocatalytic activity. Meanwhile, the Si-O bridge provides an interfacial electronic pathway that facilitates recombination of photogenerated electrons in the CB of NFONS and the holes in the VB of CNNS. Consequently, the Z-scheme mechanism enhance reducing capability of the electrons in the CB of CNNS, while the holes in the VB of NFONS have oxidation ability. Remarkably, the excited electrons work for CO_2 reduction and H_2 generation, while the retained holes and generated reactive oxygen species contribute to 2,4-DCP degradation under visible-light irradiation[43]. The equations describing the photocatalytic process initiated

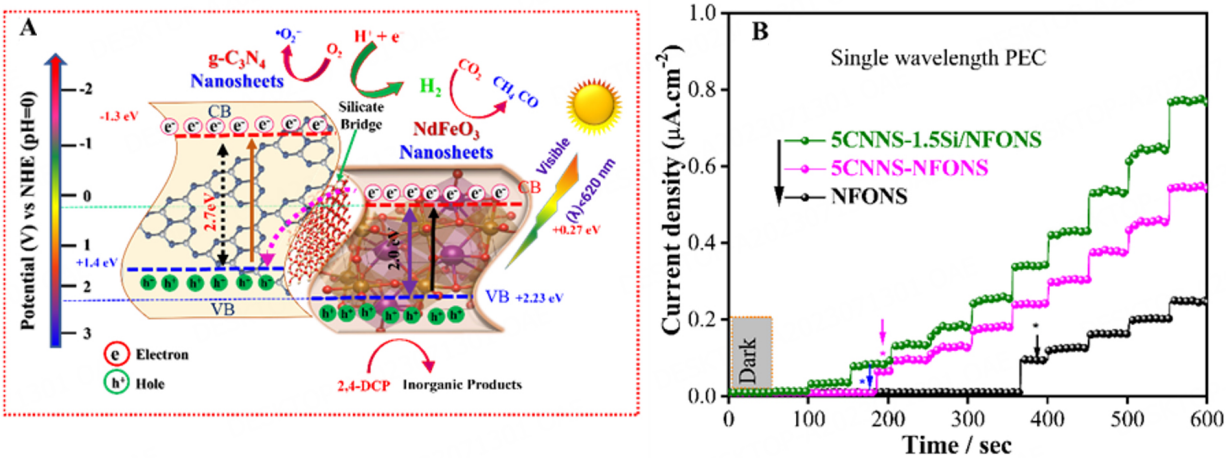


Figure 6. Schematic illustration for the establishment of Z-scheme (A) and single-wavelength photocurrent action spectra (B) for Si-bridge-mediated g-C_3N_4/$NdFeO_3$ Z-scheme heterojunction.

under visible light over the Si-Bridge-mediated g-C_3N_4/$NdFeO_3$ Z-scheme heterojunction for CO_2 conversion are given in Supplementary Table 3. These findings were further supported by single-wavelength photocurrent action spectra measurements under visible light with different modulation periods up to 600 s[44]. It can be confirmed from Figure 6B that the optimized 5CNNS-1.5Si/NFONS sample has a photocurrent response compared to pristine 5CNNS/NFONS and NFONS, which means that coupling of CNNS and introduction of a Si-O bridge enhanced charge separation, promoted electron generation, and photoelectrons modulations occurred, and a Z-scheme heterojunction has been established.

A CO_2 temperature-programmed desorption (CO_2-TPD) analysis was performed to evaluate the CO_2 capturing behavior of the prepared photocatalysts. The CO_2-TPD profiles given in Figure 7A show two main desorption peaks at approximately 200 and 650 °C, corresponding to physisorption and chemisorption of CO_2, respectively[45]. It can be observed that, compared with pristine NFONS, the 5CNNS/NFONS samples exhibit high CO_2 adsorption/desorption intensity, and as expected, the 5CNNS-1.5Si/NFONS shows the strongest CO_2 adsorption capacity. Remarkably, this enhanced capability facilitates CO_2 capture and promotes organic-pollutant adsorption on their surfaces. Furthermore, XPS analysis was performed to determine the elemental composition and oxidation states of the prepared samples.

The XPS survey Figure 7B and spectrum [Supplementary Figure 6A and B] confirmed the presence of Nd, Fe, O, C, N, and Si, confirming that the Si-bridge-mediated g-C_3N_4/$NdFeO_3$ Z-scheme heterojunction was successfully prepared. In the pristine NFONS sample, the Nd 3d XPS spectrum showed two peaks at 982.97 and 1,002.02 eV, corresponding to the Nd 3d5/2 and Nd 3d3/2 energy levels, respectively, while the Fe 2p spectrum showed two peaks at 710.30 eV (Fe 2p3/2) and 723.20 eV (Fe 2p1/2), confirming that the Fe ions are in the +3 oxidation state. Upon formation of 5CNNS/NFONS, these peaks shifted slightly to the left. The O1s spectra also showed two strong peaks at around 529.5 and 531.5 eV. These peaks originate from the lattice oxygen and surface chemisorbed oxygen (OH), respectively.

Additionally, the N1s peak observed near 399.0 eV corresponds to sp^2-hybridization of nitrogen that is linked to carbon (C-N=C). The C 1s peak at approximately 288.60 eV is associated with sp^2-hybridized carbon atoms that are bonded to nitrogen in aromatic structures (N-C=N). In addition, the XPS spectrum of the pristine Si-O bridge clearly indicates the binding energy of Si 2p. It can be noticed that a gradual positive shift in the Nd 3d and Fe 2p binding energies was observed after incorporation of CNNS and the Si-O bridge into the main NFONS sample. Although differential charging effects may influence absolute binding-energy

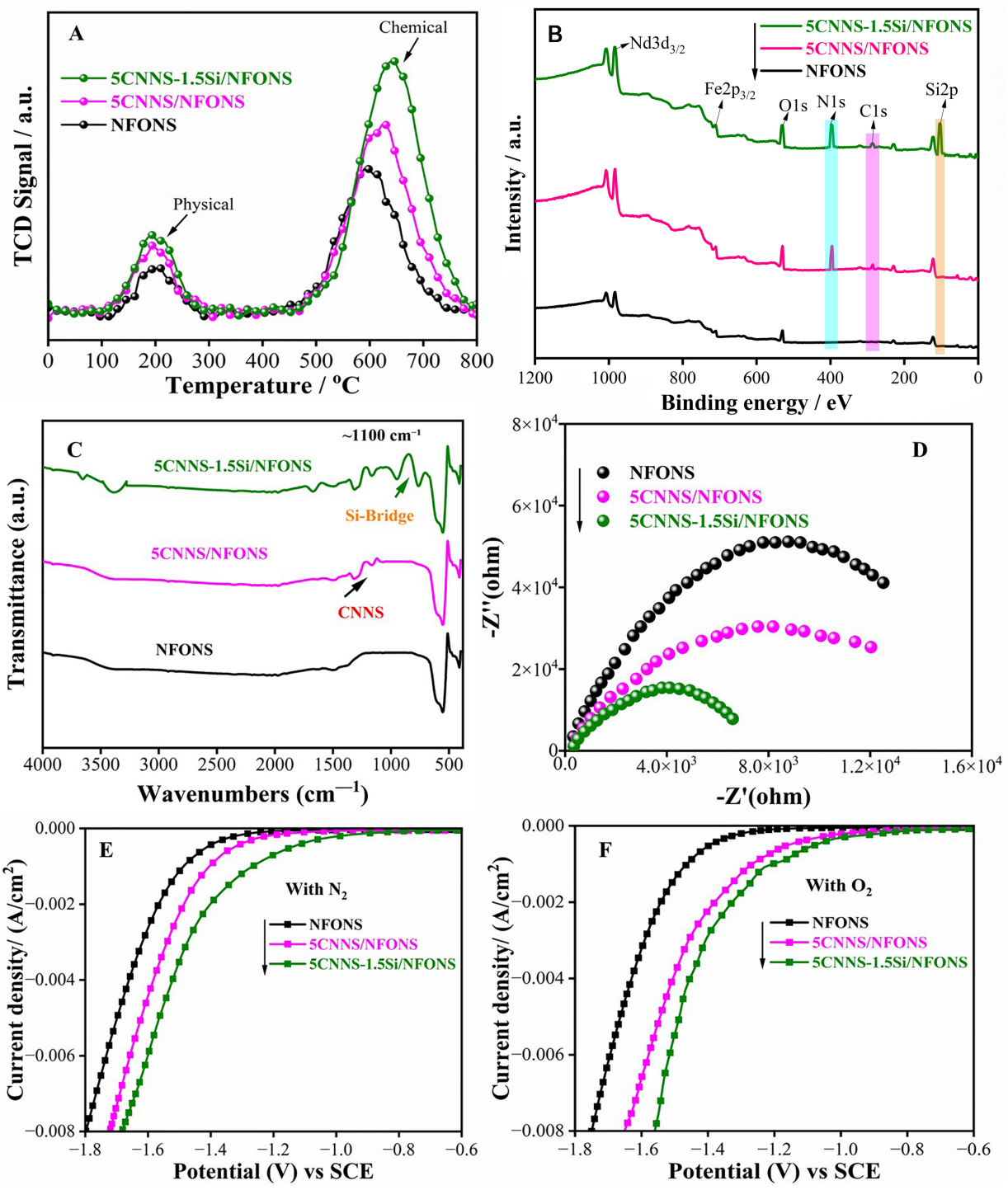


Figure 7. CO_2-TPD (A), XPS survey spectra (B), FTIR patterns (C), Nyquist plots under light irradiation (D), electrochemical (EC) reduction curves in N_2 (E) and O_2 (F) of NFONS, 5CNNS/NFONS, and 5CNNS-1.5Si/NFONS nanocomposites.

positions, the consistent relative shifts among the samples suggest changes in the local electronic environment and interfacial charge redistribution[46]. These electronic variations are consistent with interfacial interactions between CNNS, the Si-O bridge, and $NdFeO_3$, which enhance charge separation and support the proposed Z-scheme charge-transfer pathway. So, these results validate the successful integration of CNNS and the Si-O bridge within the NFONS.

Moreover, the fourier-transform infrared spectroscopy (FTIR) spectra in Figure 7C show distinct peaks between 1,100, 1,500 and 3,600 cm^{-1}, confirming the presence of the desired elements (Nd, Fe, O, N, Si, C) and functional groups[47]. Furthermore, the FTIR spectra of pristine g-C_3N_4 and the silicate bridge shown in Supplementary Figure 7B confirmed the successful synthesis of CNNS and the Si-O bridge. In short, these findings confirm that the silicate-bridged, incorporated, and g-C_3N_4-coupled $NdFeO_3$ nanosheet-based Z-scheme heterojunction was successfully fabricated.

The Nyquist plots [Figure 7D] illustrate the electrochemical performance of pristine NFONS after adding CNNS and Si-O. As expected, the 5CNNS/NFONS and 5CNNS-1.5Si/NFONS show the highest response[42]. It is widely known that a smaller semicircle radius indicates lower interfacial charge-transfer resistance. Thus, the 5CNNS-1.5Si/NFONS is the most favorable sample for efficient separation of photogenerated electron-hole pairs. The electrochemical (EC) reduction curves conducted under N_2 gas [Figure 7E] and O_2 gas [Figure 7F] reveal that the photocurrent density of NFONS shows a notable increase after adding CNNS and Si-O[48]. From EC measurements, it is concluded that O_2 acts as a sacrificial electron acceptor; the positive change in photocurrent observed under O_2 reflects photogenerated electrons available for reduction reactions, directly supporting the CO_2 reduction and H_2 generation. The holes are available for the oxidative reaction and 2,4-DCP degradation.

Furthermore, the BET surface areas of as-prepared samples were analyzed as given in Supplementary Figure 8. The optimal sample, 5CNNS-1.5Si/NFONS, showed the largest surface area (120.6 m^2/g), compared with 5CNNS/NFONS (108.9 m^2/g) and NFONS (79.2 m^2/g). Logically, the enlarged surface area provides a higher number of active sites, facilitating more effective adsorption of gas molecules and organic pollutant degradation[49]. Similarly, increased surface area enables better water molecule adsorption and efficient electron-hole pair separation, which are essential for photocatalytic H_2 generation[50].

In addition, the different pathways for photocatalytic CO_2 conversion into different valuable products over 5CNNS-1.5Si/NFONS were calculated using DFT [Figure 8A]. The initial step involves the capturing of CO_2 over 5CNNS-1.5Si/NFONS. In the next step, the CO_2 molecule experiences activation through N—C=O—Ov bonding, thereby lowering the energy barrier for CO_2 reduction[51]. The CO_2* is reduced to CO*, part of which desorbs as CO(g) as a byproduct. The remaining CO* is protonated at the Fe sites of $NdFeO_3$ to form COOH*, the only uphill step in the free-energy profile (ΔG = 0.70 eV) and therefore the potential-determining step, so the ΔG values describe the reaction thermodynamics [Figure 8B][52,53].

Subsequently, the COOH* intermediate is subjected to hydrogenation, resulting in the formation of HCOOH*, which is then further reduced to HCO*. The HCO* intermediate is subsequently transformed into H_2CO*, an essential intermediate in the methane synthesis pathway. The final reduction steps generate CH_4 from H_2CO*, with CH_4 detaching from the surface, facilitated by weak Fe-CH_4 interactions. The necessary protons (H^+) for the hydrogenation steps are mainly supplied through oxidation reactions driven by the holes retained in the VB of NFONS, which is consistent with the proposed Z-scheme charge-transfer pathway[54]. This pathway emphasizes the effective reduction of CO_2 to CH_4 and provides valuable insights that facilitate hydrogenation and influence product selectivity[55].

Furthermore, the 2,4-DCP degradation pathways are investigated over 5CNNS-1.5Si/NFONS [Figure 9]. It can be confirmed that 2,4-DCP degradation via the mineralization process involves the gradual breakdown of the aromatic compound into smaller molecules, ultimately resulting in the release of less hazardous inorganic minerals[56].

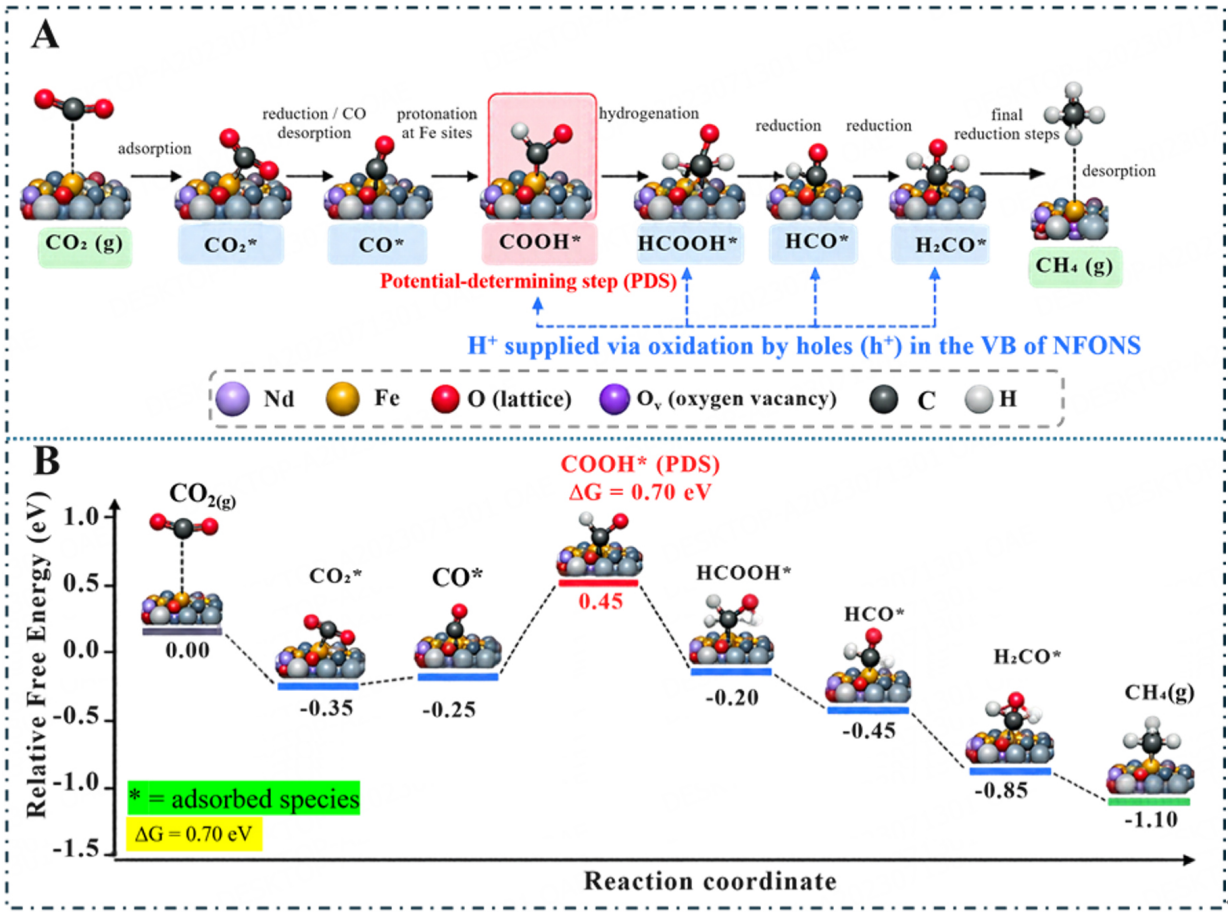


Figure 8. CO_2 conversion and reaction mechanism pathways (A) and Relative free-energy profile (B) over 5CNNS-1.5Si/NFONS.

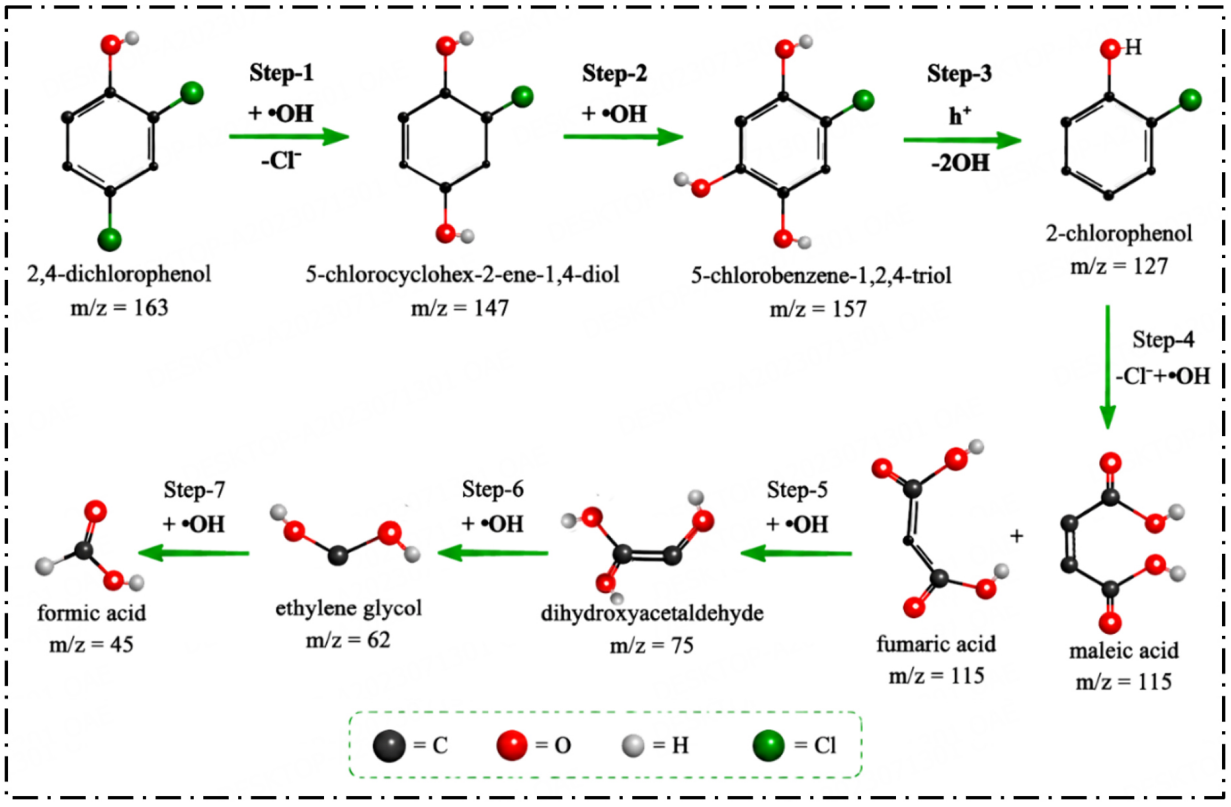


Figure 9. 2,4-DCP degradation process into inorganic minerals and mechanistic pathways over Si-bridge-mediated g-C_3N_4/$NdFeO_3$ nanocatalyst.

To verify the aforementioned 2,4-DCP degradation process, free-radical trapping (scavenger) experiments were carried out to check the most active species responsible for 2,4-DCP degradation. Generally, EDTA-2Na, isopropyl alcohol (IPA), and BQ were used to quench h^+, •OH, and $•O_2^-$, respectively, under optimized experimental parameters and conditions[57,58]. Supplementary Figure 9 shows that the photocatalytic activities of 5CNNS-1.5Si/NFONS (Optimized sample) for 2,4-DCP degradation were notably hindered by the presence of EDTA-2Na and BQ. Notably, it can be observed that 2,4-DCP degradation decreased from 87% (no scavenger) to 44% with EDTA-2Na and 59% with BQ, whereas IPA caused only a minor decrease to 83%, indicating that h^+ and $•O_2^-$ are the primary reactive species responsible for 2,4-DCP degradation.

CONCLUSION

In this research, we successfully developed a Si-bridge-mediated g-C_3N_4/$NdFeO_3$ Z-scheme heterojunction and used it for multifunctional applications. Our prepared samples showed extraordinary performance in photocatalytic CO_2 conversion, 2,4-DCP degradation, and hydrogen (H_2) generation. Compared with NFONP and CNNP, the NFONS and CNNS, respectively, have larger surface areas, more developed morphologies, enhanced charge separation, and improved photocatalytic performance. Compared with pristine NFONS, the optimized 5CNNS-1.5Si/NFONS nanocomposites delivered a 14.17-fold improvement in CO_2 conversion activities, a 7.25-fold increase for photocatalytic 2,4-DCP degradation, and a 2.64-fold increase in methanol-assisted H_2 generation. Additionally, our samples showed good stability, highlighting their potential for practical applications. The computational methodologies, DFT calculations, scavenger experiments, and reaction pathways provide more explanation and insight into the photocatalytic process, morphology modification, and photoelectron modulation. Finally, our research findings will provide a gateway to the design of $NdFeO_3$ and g-C_3N_4-based nanomaterials for their employment in environmental remediation and energy fuels production.

DECLARATIONS

Authors' contributions

Writing - original draft, investigation, conceptualization, resources, supervision: Khan, I.; Zaman, S.
Validation, investigation, software, review & editing: Kumar, A.
Resources, supervision: Bahadur, A.
Investigation, data curation: Bibi, S.
Methodology, investigation: Zaman, M. H.; Mujahid, L.; Khan, A.
Methodology, software: Yasin, G.
Data analysis, review & editing: Khan, S.

Availability of data and materials

The data supporting the findings of this study are available within this Article and its Supplementary Materials. Further data are available from the corresponding authors upon request.

AI and AI-assisted tools statement

Not applicable.

Financial support and sponsorship

This work was financially supported by the School of Chemical Science and Engineering, Tongji University, Shanghai 200092, China; the International Collaborative Research Program (ICRP2023008); and the Internal Faculty/Staff Research Support Programs (IRSPC2024007), Wenzhou-Kean University, Zhejiang 325060, China.

Conflicts of interest

All authors declared that there are no conflicts of interest.

Ethical approval and consent to participate

Not applicable.

Consent to publish

Not applicable.

Copyright

© The Author(s) 2026.

Supplementary Materials

Supplementary Materials

REFERENCES

1. Baghdadi, Y.; Daboczi, M.; Temerov, F.; Yang, M.; Cui, J.; Eslava, S. A g-C_3N_4/rGO/$Cs_3Bi_2Br_9$ mediated Z-scheme heterojunction for enhanced photocatalytic CO_2 reduction. *J. Mater. Chem. A.* **2024**, *12*, 16383-95. DOI PubMed PMC
2. Zhao, Z.; Li, P.; Liu, Y.; Song, N.; Cui, Y.; Zheng, Y. Insights into 2,4-dichlorophenol degradation by periodate activated with carbonized polyaniline-doped semi-coke. *J. Environ. Chem. Eng.* **2025**, *13*, 120111. DOI
3. Iqbal, M. U.; Rana, S.; Zitnan, M.; et al. Noble metal-free zeolitic imidazolate framework-based composite for photocatalytic production of green hydrogen. *Microstructures* **2026**, *6*, 20260107. DOI
4. Awogbemi, O.; Desai, D. A. Novel technologies for CO_2 conversion to renewable fuels, chemicals, and value-added products. *Discover. Nano.* **2025**, *20*, 29. DOI PubMed PMC
5. Ghourichay, S. A.; Ricci, P. C. Advances in carbon based nanomaterials for photocatalytic environmental remediation and solar fuel production. *Discov. Mater.* **2026**, *6*, 228. DOI
6. Li, X.; Wen, J.; Low, J.; Fang, Y.; Yu, J. Design and fabrication of semiconductor photocatalyst for photocatalytic reduction of CO_2 to solar fuel. *Sci. China. Mater.* **2014**, *57*, 70-100. DOI
7. Zhao, Y.; Zhang, J.; Ma, F.; et al. Computational exploration of two-dimensional vacancy-free boridene sheet and its derivatives: high stabilities and the promise for hydrogen evolution reaction. *Microstructures* **2024**, *4*, 2024032. DOI
8. Meng, L.; Qu, Y.; Jing, L. Recent advances in BiOBr-based photocatalysts for environmental remediation. *Chin. Chem. Lett.* **2021**, *32*, 3265-76. DOI
9. Akpasi, S. O.; Smarte Anekwe, I. M.; Tetteh, E. K.; Amune, U. O.; Mustapha, S. I.; Kiambi, S. L. Hydrogen as a clean energy carrier: advancements, challenges, and its role in a sustainable energy future. *Clean. Energy.* **2025**, *9*, 52-88. DOI
10. Li, X.; Zhou, H.; Huang, L.; et al. Detection of formaldehyde sensitive properties of Sm^{3+} doped $NdFeO_3$. *J. Alloys. Compd.* **2025**, *1010*, 176933. DOI
11. Shoukat, R.; Hussain, S.; Ata, S.; et al. Lattice oxygen-mediated ABO_3-type $NdFeO_3$ perovskite fabricated over multi-walled CNTs for the O_2 evolution reaction and photo-induced degradation of Victoria blue B. *RSC. Adv.* **2026**, *16*, 58346-59. DOI PubMed PMC
12. Yadav, P.; Pandey, A.; Khan, B.; et al. Detailed investigation on structural, optical, dielectric and magneto-dielectric properties with enhanced magneto-impedance characteristic of $NdFeO_3$ nanoparticles. *Mater. Chem. Phys.* **2023**, *309*, 128424. DOI
13. Fu, C.; Li, H.; Jiang, J.; et al. Building ultrathin nanosheet $CeVO_4$/WO_3·H_2O Z-scheme heterojunction for boosting photocatalytic CO_2 reduction. *Chem. Eng. J.* **2025**, *519*, 165194. DOI
14. Khan, I.; Luo, M.; Guo, L.; et al. Synthesis of phosphate-bridged g-C_3N_4/$LaFeO_3$ nanosheets Z-scheme nanocomposites as efficient visible photocatalysts for CO_2 reduction and malachite green degradation. *Appl. Catal. A. Gen.* **2022**, *629*, 118418. DOI
15. Zaman, S.; Khan, I.; Zhang, F.; et al. Synthesis of mediator free hollow $BiFeO_3$ spheres/porous g-C_3N_4 Z-scheme photocatalysts for CO_2 conversion and Alizarin red S degradation. *Mater. Sci. Semicond. Process.* **2023**, *162*, 107534. DOI
16. Zhao, W.; She, T.; Zhang, J.; et al. A novel Z-scheme CeO_2/g-C_3N_4 heterojunction photocatalyst for degradation of bisphenol A and hydrogen evolution and insight of the photocatalysis mechanism. *J. Mater. Sci. Technol.* **2021**, *85*, 18-29. DOI
17. Huang, R.; Wu, J.; Zhang, M.; Liu, B.; Zheng, Z.; Luo, D. Strategies to enhance photocatalytic activity of graphite carbon nitride-based photocatalysts. *Mater. Des.* **2021**, *210*, 110040. DOI
18. Gao, Y.; Sun, L.; Bian, J.; Zhang, Z.; Li, Z.; Jing, L. Accelerated charge transfer of g-C_3N_4/$BiVO_4$ Z-scheme 2D heterojunctions by controllably introducing phosphate bridges and Ag nanocluster co-catalysts for selective CO_2 photoreduction to CO. *Appl. Surf. Sci.* **2023**, *610*, 155360. DOI

19. Acharya, S.; Kandi, D.; Parida, K. CdS QD decorated $LaFeO_3$ nanosheets for photocatalytic application under visible light irradiation. *ChemistrySelect* **2020**, *5*, 6153-61. DOI
20. Wang, L.; Wu, J. A review of recent progress in silver silicate-based photocatalysts for organic pollutant degradation. *Inorg. Chem. Commun.* **2021**, *129*, 108619. DOI
21. Kherief, Y.; Omari, M.; Makhloufi, S. Synthesis and catalytic properties of Ni-doped $NdFeO_3$. *Inorg. Chim. Acta.* **2024**, *566*, 122028. DOI
22. Yao, X.; Zhang, W.; Huang, J.; et al. Enhanced photocatalytic nitrogen fixation of Ag/B-doped g-C_3N_4 nanosheets by one-step in-situ decomposition-thermal polymerization method. *Appl. Catal. A. Gen.* **2020**, *601*, 117647. DOI
23. Wu, J.; Xiong, L.; Hu, Y.; et al. Organic half-metal derived erythroid-like $BiVO_4$/hm-C_4N_3 Z-scheme photocatalyst: reduction sites upgrading and rate-determining step modulation for overall CO_2 and H_2O conversion. *Appl. Catal. B. Environ.* **2021**, *295*, 120277. DOI
24. Hosakote Shankara, A.; Samuel Prabagar, J.; Tenzin, T.; Yadav, S.; Anil Kumar, K. M.; Shivaraju, H. P. Facile synthesis of $NdFeO_3$ perovskite for photocatalytic degradation of organic dye and antibiotic. *Mater. Today. Proc.* **2023**, *75*, 15-23. DOI
25. Liu, E.; Chen, J.; Ma, Y.; et al. Fabrication of 2D SnS_2/g-C_3N_4 heterojunction with enhanced H_2 evolution during photocatalytic water splitting. *J. Colloid. Interface. Sci.* **2018**, *524*, 313-24. DOI
26. Nguyen, T. A.; Pham, V.; Pham, T. L.; et al. Simple synthesis of $NdFeO_3$ nanoparticles by the co-precipitation method based on a study of thermal behaviors of Fe (III) and Nd (III) hydroxides. *Crystals* **2020**, *10*, 219. DOI
27. Ma, J.; Wei, Z.; Li, L.; Ma, L.; Li, C.; Huang, S. Synthesis and photoelectrochemical properties of visible-light response g-C_3N_4@CdS heterojunctions photocatalyst. *Desalin. Water. Treat.* **2021**, *231*, 287-96. DOI
28. Pei, J.; Li, H.; Yu, D.; Zhang, D. g-C_3N_4-based heterojunction for enhanced photocatalytic performance: a review of fabrications, applications, and perspectives. *Catalysts* **2024**, *14*, 825. DOI
29. Liu, L.; Chen, F.; Wu, J.; Li, W.; Chen, J.; Yu, H. Fine tuning of phosphorus active sites on g-C_3N_4 nanosheets for enhanced photocatalytic decontamination. *J. Mater. Chem. A.* **2021**, *9*, 10933-44. DOI
30. Tong, S.; Liu, Z.; Lin, Y.; Yang, C. Highly enhanced photocatalytic performances of composites consisting of silver phosphate and N-doped carbon nanomesh for oxytetracycline degradation. *Int. J. Environ. Res. Public. Health.* **2022**, *19*, 14865. DOI PubMed PMC
31. Guo, J.; Ma, S.; Ma, N.; et al. Hydrothermal synthesis of $NdFeO_3$ nanoparticles and their high gas-sensitive properties. *Ceram. Int.* **2024**, *50*, 43654-64. DOI
32. Alrashidi, K. A.; Manzoor, I.; Abid, A. G.; et al. Synergistic electrochemical performance of $NdFeO_3$/rGO composite for enhanced oxygen and hydrogen evolution reactions. *J. Electroanal. Chem.* **2025**, *976*, 118807. DOI
33. Zhang, S.; Qu, Y.; Zhang, D.; et al. Rational design and biological application of hybrid fluorophores. *Chem. A. Eur. J.* **2024**, *30*, e202303208. DOI
34. Wang, Y.; Wang, L.; Wu, Z. Fabrication of phosphorus-doped g-C_3N_4/SnS nanocomposite photocatalysts for degradation of Rhodamine B under light emitting diode irradiation. *J. Mater. Sci. Mater. Electron.* **2024**, *35*, 2131. DOI
35. Xiao, M.; Luo, B.; Wang, S.; Wang, L. Solar energy conversion on g-C_3N_4 photocatalyst: light harvesting, charge separation, and surface kinetics. *J. Energy. Chem.* **2018**, *27*, 1111-23. DOI
36. Wu, G.; Wang, Q.; Ren, Q.; Mo, Z.; Xu, H. Molecular structure engineering of graphitic carbon nitride for photocatalytic hydrogen evolution: recent advances and perspectives. *Small* **2025**, e2503954. DOI PubMed
37. Ma, N.; Quan, X.; Zhang, Y.; Chen, S.; Zhao, H. Integration of separation and photocatalysis using an inorganic membrane modified with Si-doped TiO_2 for water purification. *J. Membr. Sci.* **2009**, *335*, 58-67. DOI
38. Niu, Y.; Hu, F.; Xu, H.; et al. Exploration for high performance g-C_3N_4 photocatalyst from different precursors. *Mater. Today. Commun.* **2023**, *34*, 105040. DOI
39. Zhao, J.; Ji, M.; Chen, H.; et al. Interfacial chemical bond modulated $Bi_{19}S_{27}Br_3$/g-C_3N_4 Z-scheme heterojunction for enhanced photocatalytic CO_2 conversion. *Appl. Catal. B. Environ. Energy.* **2022**, *307*, 121162. DOI
40. Hu, Q.; Yue, B.; Su, W.; et al. Syntheses, characterization, magnetic, and electrochemical properties of perovskite-type $NdFeO_3$ and $NdCoO_3$ nanofibers. *J. Am. Ceram. Soc.* **2022**, *105*, 6732-43. DOI
41. Hu, K.; Li, Z.; Chen, S.; et al. Synthesis of silicate-bridged heterojunctional SnO_2/$BiVO_4$ nanoplates as efficient photocatalysts to convert CO_2 and degrade 2,4-dichlorophenol. *Part. Part. Syst. Charact.* **2017**, *35*, 1700320. DOI
42. Benyoussef, M.; Nassereddine, Y.; Kotbi, A.; et al. Au-decorated $NdFeO_3$/g-C_3N_4 type II heterojunction photoanodes for enhanced hydrogen evolution: Integrated computational and experimental insights. *J. Power. Sources.* **2026**, *663*, 238855. DOI
43. Khan, A.; Sadiq, S.; Khan, I.; et al. Preparation of visible-light active MOFs-perovskites (ZIF-67/$LaFeO_3$) nanocatalysts for exceptional CO_2 conversion, organic pollutants and antibiotics degradation. *Heliyon* **2024**, *10*, e27378. DOI PubMed PMC

44. Nishijima, Y.; Ueno, K.; Yokota, Y.; Murakoshi, K.; Misawa, H. Plasmon-assisted photocurrent generation from visible to near-infrared wavelength using a Au-nanorods/TiO_2 electrode. *J. Phys. Chem. Lett.* **2010**, *1*, 2031-6. DOI

45. Yang, Z.; Yang, X.; Ding, X.; Li, P. CoO/Co_3O_4 heterostructures with intimate contact promote photocatalytic CO_2 reduction. *RSC. Adv.* **2026**, *16*, 22559-63. DOI PubMed PMC

46. Liu, C.; Li, C.; Fu, X.; Raziq, F.; Qu, Y.; Jing, L. Synthesis of silicate-bridged ZnO/g-C_3N_4 nanocomposites as efficient photocatalysts and its mechanism. *RSC. Adv.* **2015**, *5*, 37275-80. DOI

47. Hao, Q.; Niu, X.; Nie, C.; et al. A highly efficient g-C_3N_4/SiO_2 heterojunction: the role of SiO_2 in the enhancement of visible light photocatalytic activity. *Phys. Chem. Chem. Phys.* **2016**, *18*, 31410-8. DOI

48. Asghar, H.; Khan, I.; Saeed, M.; Wu, P.; Khan, A. Synthesis of g-C_3N_4/$SmFeO_3$ nanosheets Z-scheme based nanocomposites as efficient visible light photocatalysts for CO_2 reduction and Congo red degradation. *J. Mater. Res.* **2023**, *38*, 2986-97. DOI

49. Sun, Z.; Fischer, J. M. T. A.; Li, Q.; et al. Enhanced CO_2 photocatalytic reduction on alkali-decorated graphitic carbon nitride. *Appl. Catal. B. Environ.* **2017**, *216*, 146-55. DOI

50. Nisar, M.; Khan, N.; Qadir, M. I.; Shah, Z. Recent advances in TiO_2-based photocatalysts for efficient water splitting to hydrogen. *Nanomaterials* **2025**, *15*, 984. DOI PubMed PMC

51. Khan, I.; Yasin, G.; Kumar, A.; Wang, C.; Bahadur, A. CO_2 conversion into energy rich fuels over Nascent COF decorated-lead free halide perovskites hybrid nano catalysts: experimental and computational investigation. *Energy. Environ. Mater.* **2026**, e70410. DOI

52. Kildgaard, J.; Hansen, H.; Vegge, T. DFT+*U* study of CO_2 reduction and CO oxidation on a reconstructed CeO_{2-x}(110) facet. *Mater. Today. Adv.* **2020**, *8*, 100111. DOI

53. Zhang, H.; Liu, S.; Zhou, X.; et al. Enhanced selectivity of photocatalytic CO_2 reduction to formate via tailoring the metal site. *ACS. Catal.* **2025**, *15*, 3000-7. DOI

54. Chang, H.; Khan, I.; Yuan, A.; et al. Polyarylimide-based COF/MOF nanoparticle hybrids for CO_2 conversion, hydrogen generation, and organic pollutant degradation. *ACS. Appl. Nano. Mater.* **2024**, *7*, 10451-65. DOI

55. Wei, D.; Du, Q.; Petrov, Y. V.; Wang, Q.; Cheng, S.; Wang, Y. Improving osseointegration and antibacterial ability of Nb-doped micro arc oxidized coating with rod-like hydroxyapatite crystals on titanium surface. *Microstructures* **2026**, *6*, 20260119. DOI

56. Singh Shagolsem, B.; Mohondas Singh, N. An environmentally friendly photocatalyst for the breakdown of RhB, MB, 2,4-DCP, and TCAA: reusable Fe_3O_4/Ag doped g-C_3N_4. *J. Mol. Liq.* **2024**, *413*, 125913. DOI

57. Iqbal, W.; Yu, L.; Ahmad, M.; Shirsat, S. D.; Habimana, O.; Zhong, Z. Enhanced visible-light Cr(VI) reduction over boron-doped mesoporous g-C_3N_4 nanorods. *Chem. Eng. J. Adv.* **2026**, *27*, 101301. DOI

58. Zhou, Y.; Huang, C.; Yang, L.; et al. Enhanced photodegradation of ciprofloxacin with organic photocatalyst through a ternary strategy. *Energy. Mater.* **2025**, *5*, 500010. DOI

Disclaimer/Publisher's Note: All statements, opinions, and data contained in this publication are solely those of the individual author(s) and contributor(s) and do not necessarily reflect those of OAE and/or the editor(s). OAE and/or the editor(s) disclaim any responsibility for harm to persons or property resulting from the use of any ideas, methods, instructions, or products mentioned in the content.



© The Author(s) 2026. Open Access This article is licensed under a Creative Commons Attribution 4.0 International License (https://creativecommons.org/licenses/by/4.0/), which permits unrestricted use, sharing, adaptation, distribution and reproduction in any medium or format, for any purpose, even commercially, as long as you give appropriate credit to the original author(s) and the source, provide a link to the Creative Commons license, and indicate if changes were made.